Received: 25 June 2019 | Revised: 12 July 2019 | Accepted: 3 August 2019

DOI: 10.1002/inf2.12035

ORIGINAL ARTICLE

WILEY

# Tunable self-powered n-$SrTiO_3$ photodetectors based on varying CuS-ZnS nanocomposite film (p-CuZnS, p-CuS, and n-ZnS)

**Yong Zhang** | **Xiaojie Xu** | **Xiaosheng Fang**

Department of Materials Science, Fudan University, Shanghai, China

**Correspondence**
Xiaosheng Fang, Department of Materials Science, Fudan University, Shanghai 200433, China.
Email: xshfang@fudan.edu.cn

**Funding information**
National Natural Science Foundation of China, Grant/Award Number: 51872050 11674061 11811530065; Ministry of Education Joint Fund for Equipment Pre-Research, Grant/Award Number: 6141A02033241; Science and Technology Commission of Shanghai Municipality, Grant/Award Numbers: 17520742400, 18520710800, 18520744600

**Abstract**

The heterojunction photodetector between n-$SrTiO_3$ (n-STO) and p-CuS-ZnS (p-CZS) is prepared by a simple chemical bath deposition. The p-CZS/n-STO photodetector exhibits excellent self-powered characteristics under 390-nm light illumination, including high photosensitivity (on/off ratio of 300), fast response speed (0.7/94.6 ms), and good wavelength selectivity (410-380 nm). More importantly, the self-powered n-STO photodetectors can be regulated by varying the composition of CZS film (p-CZS, p-CuS, and n-ZnS). All devices exhibit a large open-circuit voltage and show different self-powered behaviors because of the different built-in electric fields. The open-circuit voltages of the CZS/STO, CuS/STO, and ZnS/STO devices are measured to be 0.56, 0.30, and 0.35 V, respectively. This work provides a simple and effective way to fabricate tunable self-powered photodetectors by varying the composition of the nanocomposite film.

**KEYWORDS**

CuS-ZnS, photodetectors, self-powered, $SrTiO_3$

## 1 | INTRODUCTION

Photodetectors, which detect irradiation directly by transforming light into electrical signals based on photoelectric effect, have been extensively used in various applications, such as environmental monitoring, biological/chemical analysis, flame detection, and communications.[1-7] Recently, many groups are dedicated to realizing photodetectors with self-powered characteristics.[8-12] The self-powered devices can work under zero bias due to the photovoltaic effect from p-n junctions or heterojunctions under light illumination, and are particularly appealing for their miniaturization and portability. Thus, construction of effective heterojunction between different materials in demand the built-in electric field will act as a driving force to separate photogenerated electron-hole pairs efficiently, thereby generating stable photocurrent without consuming external power. P-n junction-based detectors have the advantages of wide linear range, fast response speed, low noise, and good photoelectric performance.[13-17] Significant progresses in p-n type photodetectors have been achieved with self-powered behaviors or enhanced performance.[18-23] However, it is still extremely important to fabricate self-powered photodetectors with tailorable properties, and exploring their in-depth mechanism for practical applications.

Strontium titanate ($SrTiO_3$, STO), with a typical perovskite structure, has a wide optical bandgap of 3.2 eV, high dielectric constant, low dielectric loss, and good thermal stability. Therefore, STO has attracted growing attention in recent years for the applications in the fields of electronics, machinery, and functional ceramics.[24-28] Furthermore, STO has a high photocatalytic activity, unique electromagnetic properties and redox activity, and therefore widely used in photocatalysis, water splitting, and fuel cells.[29-31] In addition, STO crystal film

is a very attractive substrate for the growth of various oxide thin films and heterointerfaces.[32-34] However, few reports are available about the STO crystal in the field of photodetectors. Zhou et al have fabricated the STO-based high-detectivity photodetectors with different metal electrodes (Pt, Ni, and Ag).[35] Among them, the Ag/STO/Ag device depicted the highest responsivity and the lowest dark current because of the largest Schottky barrier between Ag electrode and STO. Jing et al have developed the STO/$TiO_2$ heterostructure ultraviolet (UV) detector with high responsivity and large on/off ratio via a two-step in situ hydrothermal method.[36] The high responsivity and large on/off ratio of the STO/$TiO_2$ device were attributed to the enhancement in charge separation originating from the coupling effect of STO and $TiO_2$ nanocomposites. However, these efforts lack the discussion of the self-powered characteristics of STO devices. Therefore, it is worth exploring the self-powered behavior and developing the integrated features based on STO crystals.

In our recent report, we have developed a p-type transparent, highly conductive $(CuS)_X$:$(ZnS)_{1-X}$ (CZS) film via the facile, low-cost chemical bath deposition method, which consists of ZnS and CuS nanocrystallites.[37] We demonstrated that the hole conductivity can be achieved as high as 1000 S $cm^{-1}$, and the film transparency can be tailored by adjusting the concentration of the complexing agents which can reach up to 70% in the visible range of the spectrum. Xu et al fabricated the p-CuS-ZnS (p-CZS)/n-ZnO UV photodiode with a good rectifying characteristics and a self-powered feature, which showed stable and fast photoresponse.[38] Meanwhile, we demonstrated the successful fabrication of a novel wearable self-powered p-CZS/n-$TiO_2$ UV device with high performance.[39] The fiber-shaped device shows an outstanding responsivity and high photocurrent. The as-fabricated real-time wearable UV radiation sensor can read out ambient UV power density and transmits data to smart phones via wifi. These results indicate that p-CZS films can act as a promising candidate for constructing heterojunction with other semiconductor material. More importantly, the properties of CZS nanocomposite film can be easily tuned by adjusting the ZnS to CuS ratio in precursor solution. And the CZS film can grow directly on various substrates. However, these works are only limited to utilize the p-CZS film. Therefore, further research is very attractive to investigate the photoelectric properties of STO device with the composition of CZS film (p-CZS, p-CuS, and n-ZnS).

In this work, we fabricated the p-CZS/n-STO heterojunction film by a facile chemical bath deposition method. The as-fabricated CZS/STO photodetector shows an excellent self-powered behavior, including high photosensitivity (on/off ratio of 300), fast response speed (0.7/94.6 ms), and good wavelength selectivity (410-380 nm). Moreover, we have demonstrated that the photoelectric performance of such CZS/STO heterojunction photodetector can be easily regulated by adjusting the composition of the nanocomposite film (p-CZS, p-CuS, and n-ZnS). Due to the differences in built-in electric fields, each device shows different self-powered behaviors with large open-circuit voltage. In addition, under symmetrical positive and negative bias, different devices exhibit significantly different optoelectronic properties.

## 2 | RESULTS AND DISCUSSION

The CZS composite film is prepared by a simple chemical bath deposition method. Scanning electron microscopy (SEM) was employed to study the morphology of the as-prepared p-type transparent conducting CZS nanocomposite film, and the images are displayed in Figure 1. For comparison, the SEM images of ZnS and CuS films are also displayed in Figure 1. The SEM images clearly show that the CZS film (Figure 1A,D) consists of small crystal domains (less than 10 nm) of CuS and ZnS, and this morphology favors the homogeneity and smoothness of the nanocomposite film. The CuS film (Figure 1B,E) shows the protruding, granular crystals with an average size of ~80 nm, which results the larger roughness of the CuS film. The ZnS film (Figure 1C,F) consists of tiny nanocrystals with numerous larger aggregates, leading to an island-like morphology. Compared with the deposition of pristine ZnS and CuS films via solution method, the mutual nucleation and growth of ZnS and CuS nanocrystals on the same substrate in the reaction solution might have affected the growth and hence the morphology of the composite CZS films. Herein, complexing agent was utilized to balance the free ion concentration of $Zn^{2+}$ and $Cu^{2+}$ which slowed down their release rate in the chemical bath, thereby promoting the simultaneous nucleation of ZnS and CuS nanocrystals within one film. Once the $Zn^{2+}$ and $Cu^{2+}$ ions meet $S^{2-}$ ions, the growth of the homogeneous film is initiated at the surface of the substrate. The simultaneous growth of the both ZnS and CuS nanocrystal within one film might confine the size of the crystal domain and contribute to the development of the smooth film. Comparing the three films, the CuS film with large crystal domains shows good compactness while the ZnS thin film with small crystal domains shows discontinuous morphology. The CZS composite film composed of small CuS and ZnS nanoparticles resulting in a compact and uniform film. In addition, this CZS composite film can be grown in situ on various substrates (quartz, silicon, etc.) or other semiconductor materials to construct heterojunctions via facile solution process.[37-39]

Figure 2A demonstrates the X-ray diffraction (XRD) pattern of the STO crystal film. The diffraction peak for the STO crystal appearing at 22.8°and 46.5° are assigned to (100) and (200) crystal planes of cubic strontium titanate (JCPDF no. 35-0734), respectively. All the peak positions

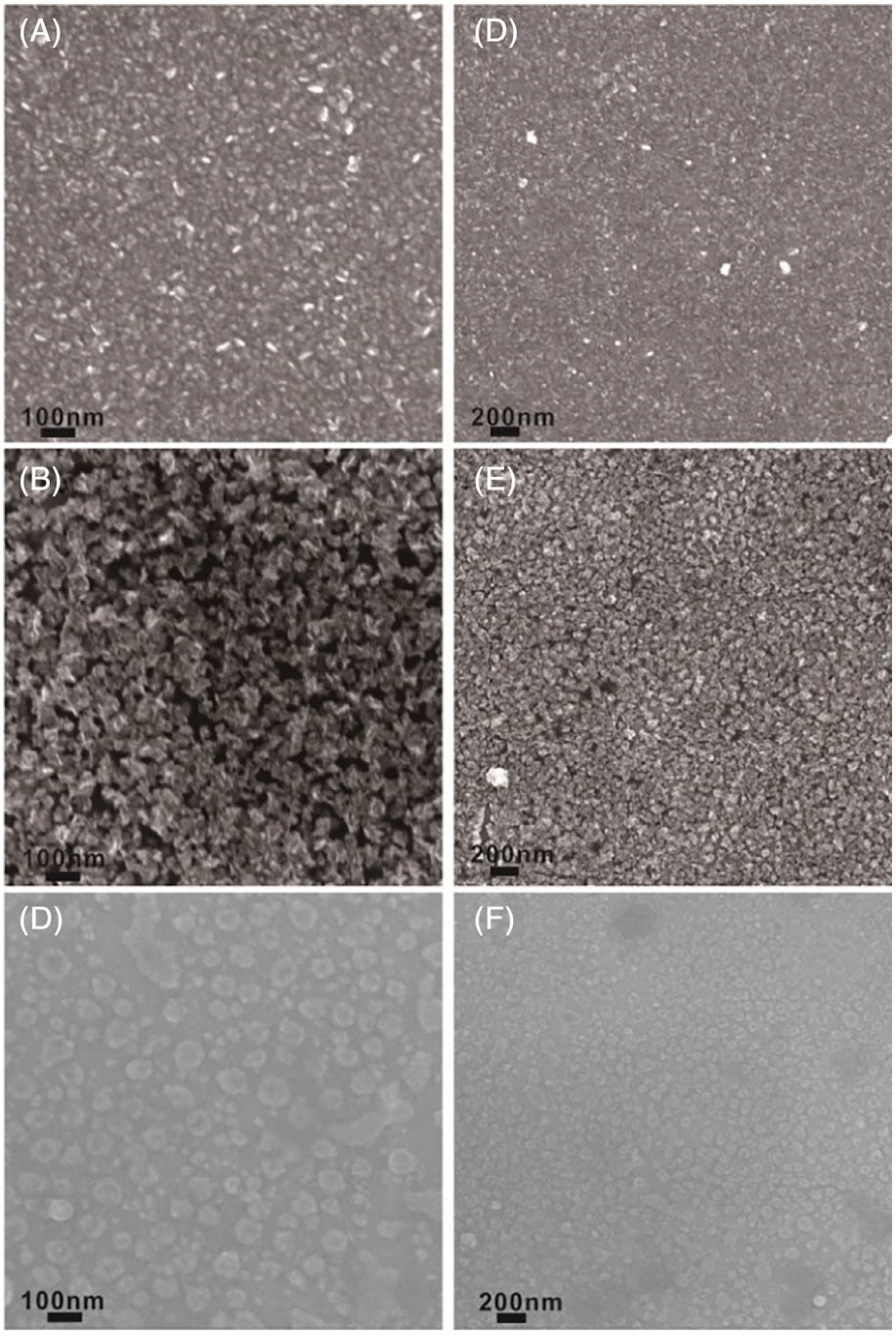


**FIGURE 1** The SEM images of the different samples in different magnification. A,D CuS-ZnS, B,E CuS, and C,F ZnS. SEM, scanning electron microscopy

and their relative intensities are in good agreement with the lattice parameters of $a = b = c = 3.905$ Å. Note that the linewidth of the peak is very small, which implies the single-crystal properties of STO film. Wide-angle X-ray scattering spectroscopy (WAXS) patterns are used to study the crystal structure of CZS films. As seen in Figure 2B, CuS film has a covellite CuS phase, and ZnS owns a sphalerite structure. The CZS film demonstrates a mixed phase of both ZnS and CuS, indicating the successful formation of the nanocomposite film. The hole conductivity of the nanocomposite film comes from the conducting network of CuS nanocrystals while the transparency is resulted from the small size of ZnS and CuS (less than 5 nm) nanocrystal domains. Furthermore, X-ray photoelectron spectroscopy (XPS) patterns were recorded to analyze the surface chemical compositions and the chemical state of each element. Figure S1a displays the full survey spectrum of the CZS film, and reveals the dominant existence of Cu, Zn, and S elements. Figure S1b,c display the full survey spectrum of the CuS and ZnS, respectively. The spectra reveal the

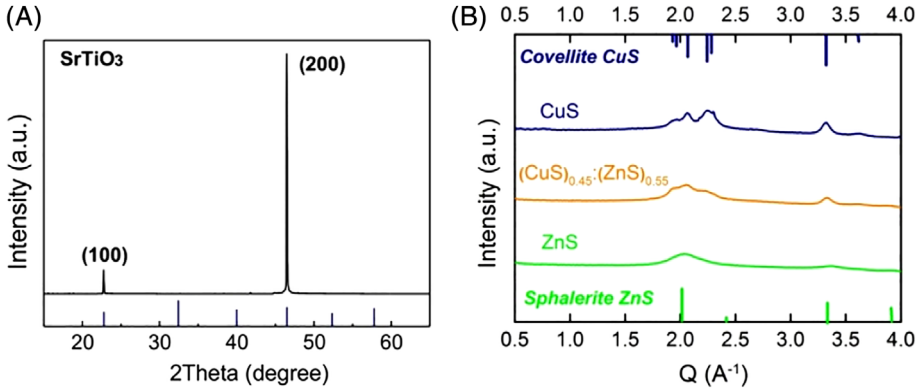


**FIGURE 2** A, XRD pattern of $SrTiO_3$. B, WAXS patterns of CuS-ZnS, CuS, and ZnS films. XRD, X-ray diffraction; WAXS, wide-angle X-ray scattering spectroscopy

dominant existence of Cu and S elements in CuS samples, and Zn and S elements in ZnS film. The binding energy peaks located at 952.2 and 932.4 eV are related to Cu $2p_{1/2}$ and Cu $2p_{3/2}$ (Figure S1d), respectively, and the splitting peaks located at 1046.5 and 1022.6 eV are assigned to Zn $2p_{1/2}$ and Zn $2p_{3/2}$ (Figure S1e), respectively. The binding energy peak located at 163.4 eV can be ascribed to S $2p_{3/2}$ (Figure S1f). These results confirm the existence of Cu, Zn, and S in CZS film. In addition, the absorption spectrum of STO film was measured to study its optical properties. As shown in Figure S2a, the sharp absorption edge of STO is at 390 nm. The optical band gap could be estimated by the Tauc plots calculated from the UV-vis absorbance spectra. As shown in Figure S2b, the band gap of STO crystal is estimated to be 3.08 eV. The optical transmittance and the band gap of CZS nanocomposite films is consistent with our previous report. ZnS film depicts a band gap of 3.6 eV, and CuS film shows an optical band gap of 2.1 eV, and <40% transmission in the visible region. The CZS film shows a peak transparency of 75% at 600 nm, and the band gaps can be tuned in the range of 2.1 to 3.6 eV by controlling the Cu composition.

In order to explore self-powered characteristics, the p-CZS composite film was integrated with n-STO crystal to construct heterojunction. Herein, half of the STO crystal film was covered with adhesive tape and immersed in precursor solution of CZS. Then the CZS film was grown on the other half of STO film (exposed part) to form a heterojunction at room temperature. The device consists of p-CZS/n-STO heterojunction with two small indium pastes as the electrodes, as illustrated in Figure 3A. The *I-V* characteristics of the CZS/STO and pure STO device in dark and under light illumination are shown in Figure 3B. The nonsymmetrical *I-V* curve of CZS/STO device in dark indicates the rectifying behavior from the p-n junction. Under 390-nm illumination (power density of 1.46 mW $cm^{-2}$), a great enhancement in current is observed and the photocurrent reaches 3 nA. To be more specific, the photocurrent of the device is about three orders of magnitude higher than that in dark at the bias of 3 V, which is slightly lower under the reverse bias. More importantly, a noticeable shift of *I-V* curve under 390-nm light illumination suggests the generation of a large open-circuit voltage (0.56 V) from the p-CZS/n-STO heterojunction. In other words, this device exhibits great potential to work in a self-powered mode, and its photocurrent can reach ~1 nA at zero bias. To understand the origin of the photovoltaic effect, *I-V* characteristics of the pure STO sample were measured and displayed in Figure 3B. A remarkable enhancement in the current under the light illumination (390 nm) is observed for pure STO. At the bias of 3 V, its photocurrent approaches to 1 nA, which is nearly two orders of magnitude higher than that in dark. Besides, the *I-V* curve shows a negligible shift between dark and illuminating conditions, indicating that it is a photoconductive-type photodetector. The symmetric *I-V* characteristic indicated the ohmic contact of n-STO and indium electrode. Therefore, the built-in electric field is believed to come from the p-n junction of p-CZS/n-STO. Compared with the optoelectronic performance of plain STO, the photocurrent of the CZS/STO device is greatly increased while the dark current is significantly decreased. There are mainly two reasons: firstly, the UV light absorption is increased from the p-CZS layer due to the presence of ZnS and CuS nanocrystal phases. Secondly, effective charge separation might have occurred at the interface of p-n junction and favored for an increased carrier lifetime resulting in the overall higher photocurrent. As a result, the ratio of photo current to dark current is greatly improved with the construction of the p-n junction. These results demonstrate that the p-CZS/n-STO device not only shows enhanced photoelectric properties, but also has self-powered characteristics.

The stability and response speed are important parameters in the characterization of photodetectors. As shown in Figure 3C, the current-time (*I-t*) characteristics of the p-CZS/n-STO device demonstrates a fast photoresponse and good repeatability without notable photocurrent decay at zero

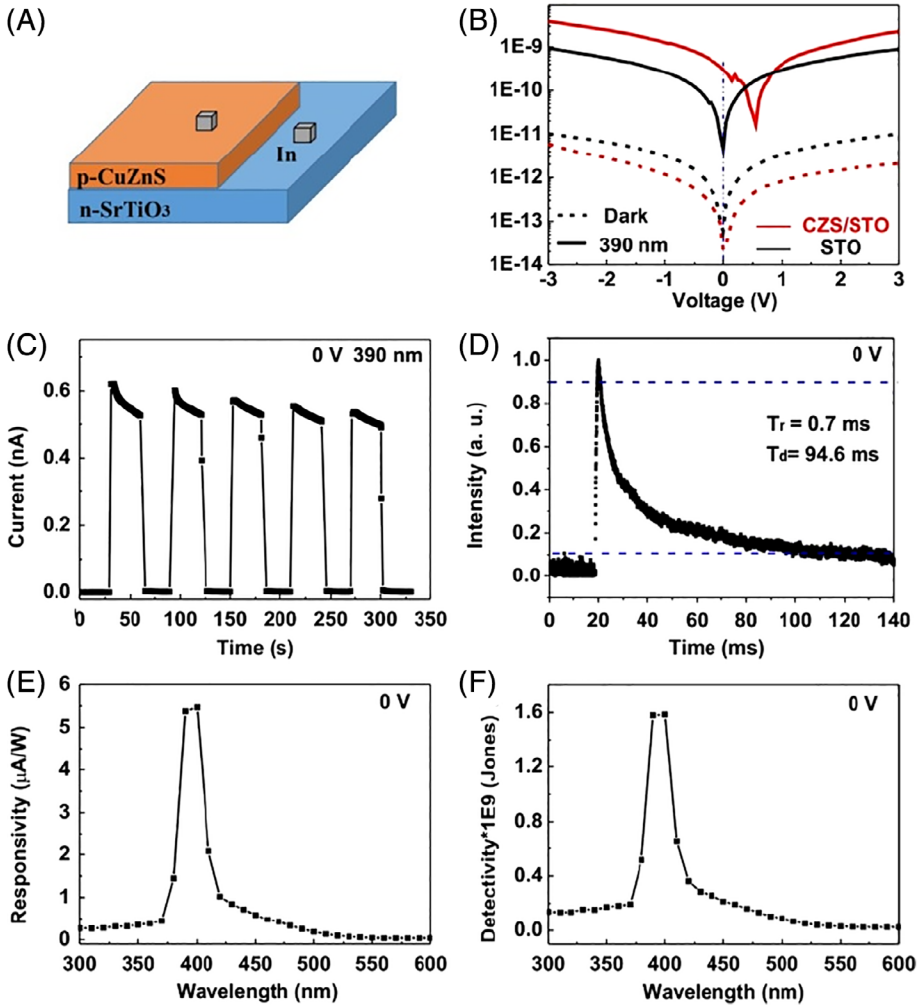


**FIGURE 3** A, Schematic illustration of the CuS-ZnS/$SrTiO_3$ device structure. B, *I-V* characteristics and C, *I-t* characteristics of the device in the dark and under 390-nm light illumination. D, The normalized *I-t* curve of pulse response, E, the responsivity, and F, detectivity characteristics of the device with irradiance wavelength ranging from 600 to 300 nm under zero bias

bias under 390-nm light illumination. The photocurrent of the device rapidly increases to a steady state and quickly decreases when the light irradiation is switched on and off without an external power supply. This indicates that the electron-hole pairs were effectively separated through the built-in electric field at the interface. The photocurrent of the composite device is achieved as high as 0.6 nA, and the dark current is as low as 2 pA. The on/off ratio, defined as the ratio of photocurrent to dark current ($I_{ph}/I_d$) of the photodetector, is calculated to be about 300 at zero bias. Moreover, the accurate time of the CZS/STO device under zero bias was recorded through a quick photoresponse measurement system. Figure 3D shows the normalized curve of the device as a function of time. The rise time (from 10% to 90%) and the decay time (from 90% to 10%) of the device are estimated to be 0.7 and 94.6 ms at zero bias, respectively. Rough preparation of the electrode and surface state of CZS film may hinder the carrier transport and recombination, thus leading to a long decay time. The corresponding optical power density of the different wavelengths of the light illumination is shown in Figure S3. The spectral responsivity ($R_\lambda$) and detectivity ($D^*$) are also key parameters to evaluate the performance of a photodetector. The responsivity is defined as the photocurrent flowing through the electrodes per incident optical power which indicates the sensitivity of a device to respond to the incident light signals. The detectivity ($D^*$, typically quoted in Jones) reflects the ability of a detector to detect weak signals from the noise environment. The responsivity and the detectivity of a device can be calculated as follows:

$$R_\lambda = \frac{I_{ph} - I_d}{P_\lambda S}, \tag{1}$$

$$D^* = \frac{R_\lambda}{(2eI_d/S)^{1/2}}, \tag{2}$$

where $I_{ph}$-$I_d$ is the difference between the photo and dark current, $P_\lambda$ is the incident irradiation power density, $e$ is the electronic charge, $\lambda$ is the excitation wavelength, and $S$ is the

effective area under light illumination, which is measured to be about 0.05 $cm^2$. As displayed in Figure 3E,F, the responsivity and detectivity of CZS/STO photodetector were calculated using incident wavelength in the ranges of 600-300 nm under 390-nm light illumination at zero bias. This device shows maximum responsivity of 5.4 μA $W^{-1}$ at 390 nm at zero bias, which is close to the band gap of STO (3.08 eV). In general, the narrowband photoresponse is related to the light penetration length and charge diffusion length.[40,41] The charge diffusion length is influenced by the thickness of crystals and the applied bias. Thanks to the thickness (0.5 mm) and single-crystalline properties of the STO film, the device exhibits a fast speed and narrowband response around at 390 nm as demonstrated in Figure S4. The composite photodetector retains such a feature with a narrowband response as the p-CZS film does not show any photoresponse. The responsivity of the device increases quickly from 420 nm (1.0 μA $W^{-1}$) to 390 nm (5.4 μA $W^{-1}$) and then decreases rapidly to 370 nm (0.45 μA $W^{-1}$) in the range of 600 to 300 nm. The cutoff wavelengths, defined as the ratio between the maximum and the natural constant ($e \approx 2.718$), are located at 410 and 380 nm (Figure 3E). The trend of the detectivity is similar to that of the responsivity with a maximum value of $1.6 \times 10^9$ Jones. The detectivity also exhibits a narrow detection band between 410 and 380 nm. These results suggest that the CZS/STO photodetector has excellent self-powered features with a large on/off ratio (300) and fast response speed (0.7/94.6 ms). It also has a good spectral selectivity. The STO single crystal has an excellent stability, and the CZS film has also shown a good stability (<300°C).[38] Therefore, the p-CZS/n-STO photodetector with high performance can be maintained for several months in the surrounding environment. As compared with two-dimensional materials (black phosphorus and InSe nanosheets), the p-CZS/n-STO device show better stability and simpler preparation.[42-44]

To have a better understanding of the large open-circuit voltage, a thorough study on the *I-V* characteristics of the p-CZS/n-STO, p-CuS/STO, and n-ZnS/STO were performed, and displayed in Figure 4A. The dark current of CZS/STO device is almost the same as that of CuS/STO but much lower than that of ZnS/STO. The three devices depict the obvious difference in photocurrents. Among them, the CZS/STO device exhibits the highest photocurrent while the ZnS/STO device exhibits the lowest photocurrent. Both the CZS/STO and CuS/STO devices show much higher photocurrent and much lower dark current than that of plain STO device. By contrary, the photocurrent of the ZnS/STO device is slightly lower than that of STO device, and the dark current is slightly higher than that of STO device. All films show negligible change between the dark and photocurrent (Figure S5). The CZS and CuS films are highly conductive p-type semiconductors while the ZnS film is n-type semiconductor with poor conductivity. The high conductivity of the CZS and CuS films is favorable for improving the photocurrent of the devices. The successful formation of p-n heterojunctions markedly reduces the dark current of the devices. Note that all the photodetectors show self-powered characteristics and large voltage offset under 390-nm illumination and are photodiode/photovoltaic devices. The open-circuit voltages of the CZS/STO, CuS/STO, and ZnS/STO

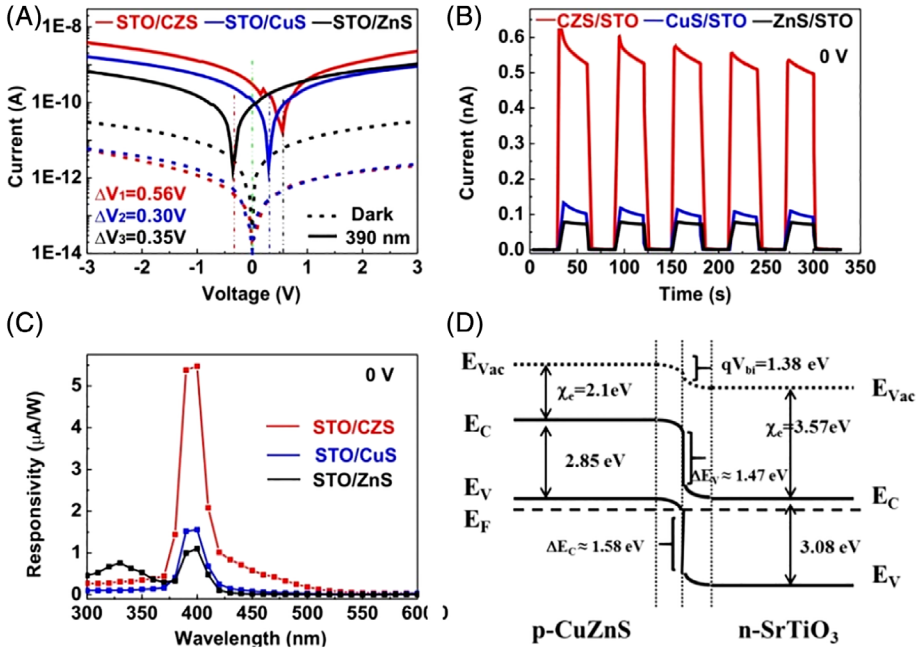


**FIGURE 4** A, *I-V* characteristics, B, *I-t* characteristics, C, the responsivities of $CuZnS/SrTiO_3$ (STO), CuS/STO, and CuS/STO photodetectors under 390-nm light illumination at zero bias. D, Schematic illustration showing the energy levels of CuZnS/STO device

devices are measured to be 0.56, 0.30, and 0.35 V, respectively. Among the three devices, CuS is a p-type semiconductor and shows a small bandgap of ~1.55 eV, which is primary cause for low-voltage offset. ZnS is expected to have good absorption around 340 nm because of its gap around 3.6 eV. However, it exhibits lower photocurrent which is attributed to the loss of carriers, an indicative of poor ZnS-STO interface. The CZS-STO device shows excellent photovoltaic effect, and maximum offset (560 mV) among all three devices, equivalent to $V_{oc}$ of a photovoltaic device. The dark current of the CZS-STO device is as low as ~1 pA at 1 V, nearly independent of film composition (ZnS/CuS/CZS). However, the light current for CZS-STO device is almost double with respect to ZnS/STO and CuS/STO at 3 V, which is attributed to the lesser surface traps/defect levels at CZS-STO interface.

In order to investigate the self-powered properties, the current-time and response characteristics of the CZS/STO, CuS/STO, and ZnS/STO devices were measured under 390-nm light illumination at zero bias, and displayed in Figure 4B,C. All devices exhibit a stable and reproducible response under 390-nm light illumination at zero bias. The current quickly rises and then falls with the light on and off for all devices. The CZS/STO device shows high sensitivity to the incident light with an on/off ratio (300) at zero bias. The CuS/STO and ZnS/STO devices both exhibit on/off ratio about 100. High on/off ratio indicates that the electron-hole pairs has been effectively generated and separated in the heterojunctions for all three devices. The responsivities under zero bias with incident wavelength ranging from 600 to 300 nm are shown in Figure 4C. The higher responsivity of the CZS/STO device than that of CuS/STO and ZnS/STO devices is attributed to its enhanced photocurrent. Furthermore, each device shows excellent spectral selectivity (380-410 nm). The responsivity peaks are appeared at 390 nm under zero bias, and the responsivity are measured to be 5.4, 1.5, and 1.0 μA $W^{-1}$ for CZS/STO, CuS/STO, and ZnS/STO devices, respectively, suggesting that STO plays a primary role in the photodetection performance for all devices. In addition, the ZnS film also contributes to the photoresponse in UV light illumination. The responsivity peak of the ZnS/STO device is centered at 340 nm which corresponds to the optical band gap of ZnS film. The pure STO film device exhibits narrow photoresponse (380-410 nm), and provides an excellent platform to integrate with other semiconductors, thereby forming the double-color self-powered photodetectors. These results demonstrate that self-powered characteristics of devices can be regulated by integrating STO film with CZS nanocomposite film of different compositions (p-CZS, p-CuS, and n-ZnS).

From UV-vis data, the bandgap of CZS film is estimated to be 2.85 eV. Room temperature Hall measurements of CZS film deposited on quartz show very high carrier concentration of the order of ~$10^{22}$ $cm^{-3}$. At this carrier concentration, the CZS film can be regarded as degenerate. Hall data reveals that the CZS film is p-type, and therefore the Fermi level lies within the valence band as shown in Figure 4D. The equilibrium band diagrams of CZS/STO interface show the conduction band and valence band offsets of about 1.47 and 1.58 eV, respectively. These offsets offer large barriers for diffusion-induced transport of electrons and holes. This explains a very low (~pA) forward current in the dark as shown in Figure 4A. At low-to-moderate forward bias in the dark, the barrier or built-in potential reduces from its equilibrium value (1.38 V). However, the conduction and valence band offsets are still large (~1 eV), which prevent the significant flow of minority carriers by diffusion. Thus, the dark current remains limited to a few pA range. In the reverse bias under dark, the Fermi level on the CZS side is pushed up with higher and higher reverse bias, it will level with the conduction band on the STO side, making high probability of electron tunneling from valence band of CZS to conduction band of STO. Effects of traps or defects at the CZS/STO interface are not considered in this band diagram. The higher current in the reverse bias for CZS-STO device in dark is very likely due to electron tunneling from valence band of CZS to conduction band of STO. Similar behavior was observed in CuS/STO device but not in ZnS/STO device. Under illumination, the wavelength of incident radiation (390 nm) is sufficient to generate excess electron-hole pairs in the CZS film (band gap ~2.85 eV) resulting an observed offset of around 500 mV. Both, CuS and CZS show similar characteristics under dark and light illumination. However, owning to larger bandgap of CZS, the CZS/STO device possesses higher open-circuit voltage than CuS-STO device. ZnS makes the film n-type resulting in an n-n + junction at higher bandgap.

To gain more insight into the photoelectric properties of the as-fabricated devices, we further investigated their photoresponses under 390-nm light illumination at the symmetric forward and reverse biases. Different biases are adopted according to the open-circuit voltage of the different devices. The binary response *I-t* characteristics of the CZS/STO, CuS/STO, and CuS/STO devices are measured at −0.55 and 0.55 V, −0.3 and 0.3 V, and −0.35 and 0.35 V under 390-nm light illumination, respectively, and displayed in Figure 5. All the devices show the stable and fast photoresponse with markedly different responses for different light at their symmetrical biases. The ratio of the photocurrent under positive bias to photocurrent under negative bias for CZS/STO, CuS/STO, and ZnS/STO devices are calculated to be 25, 30, and 20, respectively, indicating that all devices have the excellent binary responses. The on/off ratios for CZS/STO, CuS/STO, and ZnS/STO devices are measured to be 200/50, 120/20, and 2/25, respectively, at

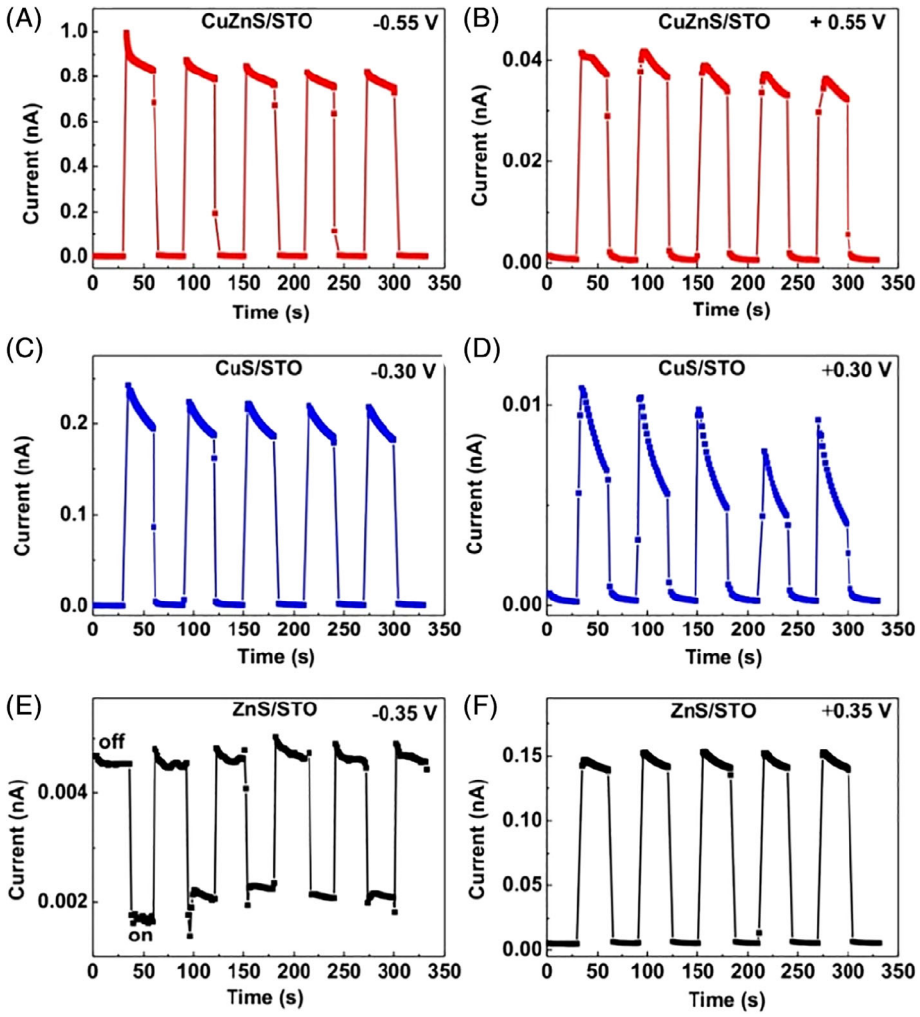


**FIGURE 5** *I-t* curves of different photodetectors under 390-nm light irradiation at theirs forward and reverse biases, respectively. A,B CuZnS, C,D CuS, and E,F ZnS

different biases. Due to higher carrier concentration, the CZS/STO device shows higher photocurrent and larger on/off ratio than that of CuS/STO and ZnS/STO devices. Interestingly, as displayed in Figure 5E,F, the photocurrent of the ZnS/STO is lower than the dark current under −0.35 V while higher than dark current under +0.35 V. The photocurrent increases when the light is turned off and decreases when the light is turned on at −0.35 V bias, showing the different trend from that of at +0.35 V. These results provide us promising candidates to design tunable self-powered photodetectors for wide practical applications based on p-CZS, p-CuS, and n-ZnS films.

## 3 | CONCLUSIONS

In summary, the p-CZS/n-STO heterojunction is prepared by a facile chemical bath deposition method. The as-fabricated CZS/STO photodetector exhibits excellent self-powered characteristics under 390-nm light illumination, including high photosensitivity (on/off ratio of 300), fast response speed (0.7/94.6 ms), and good wavelength selectivity (410-380 nm) due to photovoltaic effect. The self-powered n-STO photodetectors can be regulated by varying the composition of CZS nanocomposite film (p-CZS, p-CuS, and n-ZnS). All the devices exhibit a large open-circuit voltage and show excellent self-powered characteristics of the difference and relation. In addition, each device exhibits significantly different optoelectronic properties under symmetrical positive and negative biases because of different built-in electric fields. This work provides a simple and effective approach to fabricate tunable high-performance self-powered photodetectors.

## 4 | EXPERIMENTAL SECTION

### 4.1 | Preparation of CZS/STO heterojunction

The STO single-crystal films were purchased from Hefei Kejing Materials Technology Co., Ltd, and other chemicals

were purchased from Aladdin. The STO film has a cubic structure with (100) orientation, and a size of $10 \times 10 \times 0.5$ mm. All the chemicals were used as received without further purification. Blend solution of 50 mL of $CuSO_4$ and $Zn(CH_3COO)_2$ was prepared by dissolving in deionized water (DIW). Similarly, $Na_2EDTA$ (C10H14N2Na2O8) (0.48 g, 25 mL) and $C_2H_5NS$ (0.3 g, 25 mL) were separately prepared by dissolving in DIW. Later, 25 mL of $Na_2EDTA$ solution was added to the 50 mL blend solution of copper sulfate and zinc acetate, and mixed in ultrasonic bath for 10 minutes. Then, $C_2H_5NS$ solution was added to the mixture solution. The STO film was directly used without any treatment. Half of the STO film is covered with high temperature tape and was immediately immersed in the solution. The beaker was sealed and placed on a hot plate under slow stirring at 75°C for 1 hour. Later, the STO film was removed from the solution, washed with DIW, and dried by nitrogen. Different $(ZnS)_x$:$(CuS)_{1-x}$ nanocomposite films were achieved simply by adjusting the ZnS to CuS ratio in precursor solution. The CuS/STO and ZnS/STO heterojunction films were prepared by adjusting the solution only with $CuSO_4$ or $Zn(CH_3COO)_2$, respectively. Other experimental steps are similar to the preparation of CuZnS/STO film. Two small pieces of indium grains were doctoral bladed onto the composite film as electrodes to construct CZS/STO photodetectors. The diameter of electrodes and the channel length are about 0.17 and 0.3 cm, respectively. The active area is about 0.05 $cm^2$.

## 4.2 | Material characterization and photoelectric measurements

Sample morphologies were examined using the field-emitting-SEM (Zeiss Sigma). XRD patterns were collected on a Bruker D8-A25 diffractometer using Cu Kα radiation ($\lambda = 1.5405$ Å) in the $2\theta$ range from 10° to 70°. XPS (E Perkin Elmer PHI 5000 C ESCA system equipped with a hemispherical electron energy analyzer) was utilized to investigate the composition and chemical state of each element in the samples. The binding energy for C 1s peak at 284.6 eV was used as reference for calibration. The optical properties were characterized by a UV-vis spectrophotometer (Hitachi U-3900H). The photoelectric performance was characterized with a program-controlled semiconductor characterization system (Keithley 4200). The light intensity was measured with a NOVA II power meter (OPHIR Photonics). Time-resolved responses of the device were measured via a Nd:YAG 355-nm pulsed laser (a duration of 3-5 ns) and a digital oscilloscope. All the measurements were performed in ambient conditions.

## ACKNOWLEDGMENTS

The authors would like to thank Sandeep Kumar Maurya and Suren Patwardhan for calculating the equilibrium band diagram of p-CZS/n-STO device. The authors thank Mahesh Kumar Joshi for improvements to the English. This work was supported by National Natural Science Foundation of China (51872050, 11674061, and 11811530065), Science and Technology Commission of Shanghai Municipality (18520744600, 18520710800, and 17520742400), and the Ministry of Education Joint Fund for Equipment Pre-Research (6141A02033241).

## CONFLICT OF INTEREST

The authors declare no potential conflict of interest.

## ORCID

*Xiaosheng Fang* https://orcid.org/0000-0003-3387-4532

## REFERENCES

1. Norris D. Infrared imaging multispectral quantum-dot photodetectors. *Nat Photon*. 2019;13:230-232.
2. Cao F, Meng L, Wang M, Tian W, Li L. Gradient energy band driven high-performance self-powered perovskite/CdS photodetector. *Adv Mater*. 2019;31:1806725.
3. Cheng B, Li T, Wei P, et al. Layer-edge device of two-dimensional hybrid perovskites. *Nat Commun*. 2018;9:5196.
4. Zhang Q, Travakoli M, Gu L, et al. Efficient metal halide perovskite light-emitting diodes with significantly improved light extraction on nanophotonic substrates. *Nat Commun*. 2019;10:727.
5. Tang X, Ackerman M, Shen G, Guyot-Sionnest P. Towards infrared electronic eyes: flexible colloidal quantum dot photovoltaic detectors enhanced by resonant cavity. *Small*. 2019;15:1804920.
6. Xie C, Lu X, Tong X, et al. Recent progress in solar-blind deep-ultraviolet photodetectors based on inorganic ultrawide bandgap semiconductors. *Adv Funct Mater*. 2019;29:1806006.
7. Al-Amri A, Cheng B, He J. Perovskite methylammonium lead trihalide heterostructures: progress and challenges. *IEEE Trans Nano*. 2019;18:1-12.
8. Zhang Y, Xu W, Xu X, et al. Low-cost writing method for self-powered paper-based UV photodetectors utilizing Te/$TiO_2$ and Te/ZnO heterojunctions. *Nanoscale Horiz*. 2019;4:452-456.
9. Guo D, Su Y, Shi H, et al. Self-powered ultraviolet photodetector with superhigh photoresponsivity (3.05A/W) based on the GaN/Sn:$Ga_2O_3$ pn junction. *ACS Nano*. 2018;12:12827-12835.
10. Wang Y, Zhu L, Feng Y, Wang Z, Wang Z. Comprehensive pyrophototronic effect enhanced ultraviolet detector with ZnO/Ag Schottky junction. *Adv Funct Mater*. 2019;29:1807111.
11. Alamri A, Leung S, Vaseem M, Shamim A, He J. Fully inkjet-printed photodetector using a graphene/perovskite/graphene heterostructure. *IEEE Trans Elect Dev*. 2019;66:2657-2661.
12. Chen Y, You Y, Chen P, et al. Environmentally and mechanically stable selenium 1D/2D hybrid structures for broad-range photoresponse from ultraviolet to infrared wavelengths. *ACS Appl Mater Interf*. 2018;10:35477-35486.
13. Li S, Zhang Y, Yang W, Fang X. Solution-processed transparent $Sn^{4+}$-doped CuI hybrid photodetectors with enhanced performances. *Adv Mater Interfaces*. 2019;6:1900669.

14. Liu H, Li D, Chao M, et al. Van der Waals epitaxial growth of vertically stacked $Sb_2Te_3/MoS_2$ p-n heterojunctions for high performance optoelectronics. *Nano Energy*. 2019;59:66-74.
15. Ouyang W, Teng F, He J, Fang X. Enhancing the photoelectric performance of photodetectors based on metal oxide semiconductors by charge-carrier engineering. *Adv Funct Mater*. 2019;29:1807672.
16. Shen Y, Wei C, Ma L, et al. In situ formation of $CsPbBr_3$/ZnO bulk heterojunctions towards photodetectors with ultrahigh responsivity. *J Mater Chem C*. 2018;6:12164-12169.
17. Zhang Z, Ning Y, Fang X. From nanofibers to ordered ZnO/NiO heterojunction arrays for self-powered and transparent UV photodetectors. *J Mater Chem C*. 2019;7:223-229.
18. Ning Y, Zhang Z, Teng F, Fang X. Novel transparent and self-powered UV photodetector based on crossed ZnO nanofber array homojunction. *Small*. 2018;14:1703754.
19. Frisenda R, Molina-Mendoza AJ, Mueller T, Castellanos-Gomez A, van der Zant H. Atomically thin p-n junctions based on two-dimensional materials. *Chem Soc Rev*. 2018;47:3339-3358.
20. Teng F, Hu K, Ouyang W, Fang X. Photoelectric detectors based on inorganic p-type semiconductor materials. *Adv Mater*. 2018;30:1706262.
21. Zhang Y, Li S, Yang W, Joshi M, Fang X. Millimeter-sized single-crystal $CsPbBr_3$/CuI heterojunction for high-performance self-powered photodetector. *J Phys Chem Lett*. 2019;10:2400-2407.
22. Yang W, Hu K, Teng F, Weng J, Zhang Y, Fang X. High-performance silicon-compatible large-area UV-to-visible broadband photodetector based on integrated lattice-matched type II se/n-Si heterojunctions. *Nano Lett*. 2018;18:4697-4703.
23. Zhang Y, Xu W, Xu X, Cai J, Yang W, Fang X. Self-powered dual-color UV-green photodetectors based on $SnO_2$ millimeter wire and microwires/$CsPbBr_3$ particle heterojunctions. *J Phys Chem Lett*. 2019;10:836-841.
24. Rodenbucher C, Menzel S, Wrana D, et al. Current channeling along extended defects during electroreduction of $SrTiO_3$. *Sci Rep*. 2019;9:2502.
25. Yin X, Tan Z, Yang R, Guo X. Single crystalline $SrTiO_3$ as memristive model system: from materials science to neurological and psychological functions. *Electroceramics*. 2017;39:210-222.
26. Waser R, Dittmann R, Staikov G, Szot K. Redox-based resistive switching memories-nanoionic mechanisms, prospects, and challenges. *Adv Mater*. 2009;21:2632-2663.
27. Menzel S, Waters M, Marchewka A, Böttger U, Dittmann R, Waser R. Origin of the ultra-nonlinear switching kinetics in oxide-based resistive switches. *Adv Funct Mater*. 2011;21:4487-4492.
28. Zhang Y, Lim C, Dai Z, et al. Photonics and optoelectronics using nano-structured hybrid perovskite media and their optical cavities. *Phys Rep*. 2019;795:1-51.
29. Ruiz-Morales J, Canales-Vazquez J, Savaniu C, et al. Disruption of extended defects in solid oxide fuel cell anodes for methane oxidation. *Nature*. 2006;439:568-571.
30. Kang Q, Wang T, Li P, et al. Photocatalytic reduction of carbon dioxide by hydrous hydrazine over Au-Cu alloy nanoparticles supported on $SrTiO_3/TiO_2$ coaxial nanotube arrays. *Angew Chem Int Ed*. 2014;54:841-845.
31. Ji L, McDaniel M, Wang S, et al. A silicon-based photocathode for water reduction with an epitaxial $SrTiO_3$ protection layer and a nanostructured catalyst. *Nat Nanotech*. 2014;10:84-90.
32. Saintgirons G, Cheng J, Regreny P, et al. Accommodation at the interface of highly dissimilar semiconductor/oxide epitaxial systems. *Phys Rev B*. 2009;80:155308.
33. Neretina S, Hughes R, Devenyi G, et al. Atypical grain growth for (211) CdTe films deposited on surface reconstructed (100) $SrTiO_3$ substrates. *Appl Surf Sci*. 2009;255:5674-5681.
34. Zhang K, Wu R, Tang F, et al. Electronic structure and band alignment at the NiO and $SrTiO_3$ p-n heterojunctions. *ACS Appl Mater Interfaces*. 2017;9:26549-26555.
35. Zhou W, Jin K, Guo H, et al. Electrode effect on high-detectivity ultraviolet photodetectors based on perovskite oxides. *J Appl Phys*. 2013;114:224503.
36. Jing F, Zhang D, Li F, Zhou J, Sun D, Ruan S. High performance ultraviolet detector based on $SrTiO_3/TiO_2$ heterostructure fabricated by two steps in situ hydrothermal method. *J Alloy Comp*. 2015;650:97-101.
37. Xu X, Bullock J, Schelhas L, et al. Chemical bath deposition of p-type transparent, highly conducting $(CuS)_x$:$(ZnS)_{1-x}$ nanocomposite thin films and fabrication of Si heterojunction solar cells. *Nano Lett*. 2016;16:1925-1932.
38. Xu X, Shukla S, Liu Y, et al. Solution-processed transparent self-powered p-CuS-ZnS/n-ZnO UV photodiode. *Phys Status Solidi-R*. 2018;12:1700381.
39. Xu X, Chen J, Cai S, et al. A real-time wearable UV-radiation monitor based on a high-performance p-CuZnS/n-$TiO_2$ photodetector. *Adv Mater*. 2018;30:1803165.
40. Fang Y, Dong Q, Shao Y, Yuan Y, Huang J. Highly narrowband perovskite single-crystal photodetectors enabled by surface-chargerecombination. *Nat Photonics*. 2015;9:679-686.
41. Rao H, Li W, Chen B, Kuang D, Su C. In situ growth of 120 $cm^2$ $CH_3NH_3PbBr_3$ perovskite crystal film on FTO glass for narrowband-photodetectors. *Adv Mater*. 2017;29:1602639.
42. Li Z, Qiao H, Guo Z, et al. High-performance photoelectrochemical photodetector based on liquid-exfoliated few-layered InSe nanosheets with enhanced stability. *Adv Funct Mater*. 2018;28:1705237.
43. Ren X, Li Z, Huang Z, et al. Environmentally robust black phosphorus nanosheets in solution: application for self-powered photodetector. *Adv Funct Mater*. 2017;27:1606834.
44. Liu Y, Shivananju B, Wang Y, et al. Highly efficient and air-stable infrared photodetector based on 2D layered graphene-black phosphorus heterostructure. *ACS Appl Mater Interfaces*. 2017;9:36137-36145.


## SUPPORTING INFORMATION

Additional supporting information may be found online in the Supporting Information section at the end of this article.

**How to cite this article:** Zhang Y, Xu X, Fang X. Tunable self-powered n-$SrTiO_3$ photodetectors based on varying CuS-ZnS nanocomposite film (p-CuZnS, p-CuS, and n-ZnS). *InfoMat*. 2019;1:542–551. https://doi.org/10.1002/inf2.12035